ENGINEERING

Synthetic and living micropropellers for convection-enhanced nanoparticle transport

S. Schuerle[1], A. P. Soleimany[2,3], T. Yeh[3], G. M. Anand[3], M. Häberli[4], H. E. Fleming[3], N. Mirkhani[1], F. Qiu[4], S. Hauert[5], X. Wang[4], B. J. Nelson[4], S. N. Bhatia[3,6,7,8,9,10,11,12,13]*

Nanoparticles (NPs) have emerged as an advantageous drug delivery platform for the treatment of various ailments including cancer and cardiovascular and inflammatory diseases. However, their efficacy in shuttling materials to diseased tissue is hampered by a number of physiological barriers. One hurdle is transport out of the blood vessels, compounded by difficulties in subsequent penetration into the target tissue. Here, we report the use of two distinct micropropellers powered by rotating magnetic fields to increase diffusion-limited NP transport by enhancing local fluid convection. In the first approach, we used a single synthetic magnetic microrobot called an artificial bacterial flagellum (ABF), and in the second approach, we used swarms of magnetotactic bacteria (MTB) to create a directable "living ferrofluid" by exploiting ferrohydrodynamics. Both approaches enhance NP transport in a microfluidic model of blood extravasation and tissue penetration that consists of microchannels bordered by a collagen matrix.

INTRODUCTION

Nanoparticles (NPs) have been increasingly investigated for their potential applications as carriers in biomedical delivery techniques, because they may overcome several limitations associated with conventional drug formulations (1, 2). While they are designed to alter the pharmacokinetics and biodistribution of their associated drugs, physiological barriers to NP transport often impede their successful accumulation at diseased sites, limiting their therapeutic effect in ailments ranging from cancer to inflammation (2, 3). In the context of cancer therapy, the abnormal vessel architecture often present in tumors results in poor perfusion and high interstitial fluid pressure, both of which hinder extravasation and tumor penetration of therapeutic compounds, resulting in a persistent and prevalent obstacle in achieving effective treatment via intravenously administered interventions (4, 5).

Because the diffusion-limited transport of NPs into tissues is strongly influenced by their physicochemical properties, redesigning NP shape and surface properties to optimize transport kinetics at vessel walls and through tissues has been investigated extensively (6, 7). While small NPs exhibit higher diffusion coefficients and enhanced tissue penetration, they are rapidly cleared by renal excretion and phagocytosis. This observation has led to the proposal of multistage approaches such that some NPs have been designed to shrink or fragment over time or upon exposure to environmental cues associated with disease (8, 9). In addition, surface charge, hydrophobicity, and surface biochemistry greatly affect NP transport and have been widely subjected to optimization for more effective, passive trafficking in vivo (10).

These efforts to design NPs for improved diffusive transport have been supplemented by strategies that use external sources of energy, including magnetic and acoustic forces (11–13). While these methods show promise, scaling law effects and feasibility issues with achieving sufficient forces in deep tissue both impose limitations (11, 14). Alternatively, using external energy sources to drive microrobots has been suggested as a method to wirelessly control shuttling of NPs to diseased tissue (15–17). Several in vivo navigation strategies for microrobots have been studied (15); however, these methods still rely on diffusive transport after release of their onboard cargo. Previously, the idea that convective flow could overcome limits to diffusive transport into tumors spurred investigation into implantable devices that continuously infuse drugs via catheters, although such invasive approaches risk tissue damage and suffer from issues in establishing efficient convection patterns (18, 19).

Here, we report two distinct strategies to generate localized convective flow in a wireless fashion to circumvent the invasiveness of implanted devices. Inspired by the field of microrobots, we use either a single, synthetic, bacteria-inspired microrobot or swarms of large numbers of living bacteria to drive localized NP transport, not by directly shuttling but rather by acting as micropropellers to promote magnetically driven convection in a defined location. Both these micropropeller-based strategies are compatible with a wide range of NPs, because they do not rely on the magnetic properties of these particles. The synthetic microrobot imitates bacterial propulsion and is referred to as an artificial bacterial flagellum (ABF; Fig. 1A) (20). We also harnessed large numbers of living micropropellers by using dense swarms of magnetotactic bacteria (MTB), a naturally occurring group of Gram-negative prokaryotes that have magnetic properties (Fig. 1A) (21). With our magnetofluidic setup (Fig. 1B) (22), we show that these magnetically responsive systems increase convection in microvessel models, resulting in enhanced transport of co-delivered NPs into surrounding collagen matrices, and thereby demonstrate their potential to enhance extravasation and tissue penetration. We conclude that these physical approaches may help to overcome existing transport barriers and enhance NP tissue penetration through wirelessly controlled, spatiotemporally precise local convection.

[1]Institute for Translational Medicine, Department of Health Sciences and Technology, ETH Zurich, CH-8092 Zurich, Switzerland. [2]Harvard Graduate Program in Biophysics, Harvard University, Boston, MA 02115, USA. [3]Institute for Medical Engineering and Science, Massachusetts Institute of Technology, Cambridge, MA 02142, USA. [4]Institute of Robotics and Intelligent Systems, ETH Zurich, CH-8092 Zurich, Switzerland. [5]Engineering Mathematics, University of Bristol, Bristol BS8 1UB, UK. [6]Koch Institute for Integrative Cancer Research, Massachusetts Institute of Technology, Cambridge, MA 02139, USA. [7]Research Laboratory of Electronics, Massachusetts Institute of Technology, Cambridge, MA 02139, USA. [8]Electrical Engineering and Computer Science, Massachusetts Institute of Technology, Cambridge, MA 02139, USA. [9]Marble Center for Cancer Nanomedicine, Massachusetts Institute of Technology, Cambridge, MA 02139, USA. [10]Department of Medicine, Brigham and Women's Hospital and Harvard Medical School, Boston, MA 02115, USA. [11]Broad Institute of Massachusetts Institute of Technology and Harvard, Cambridge, MA 02139, USA. [12]Howard Hughes Medical Institute, Cambridge, MA 02139, USA. [13]Wyss Institute for Biologically Inspired Engineering at Harvard, Boston, MA 02115, USA.
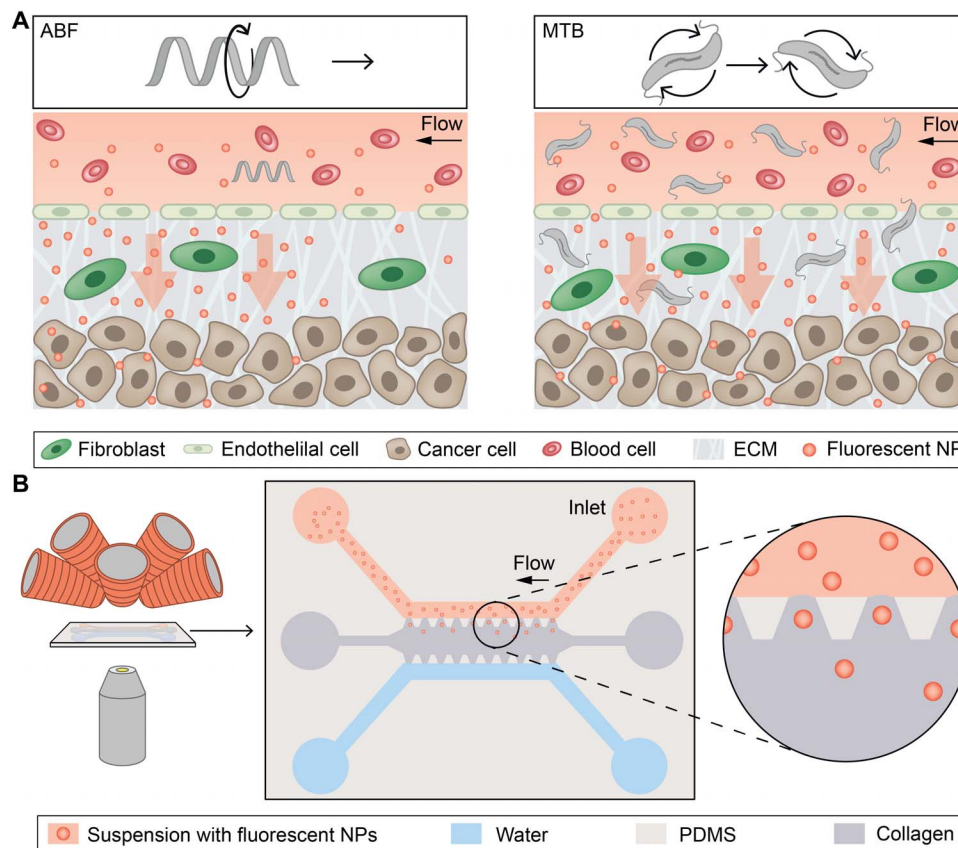*Corresponding author. Email: sbhatia@mit.edu

Fig. 1. Conceptual overview of magnetically controlled micropropellers for convection-enhanced NP transport. (**A**) Conceptual schematic depicting a single microrobot, the ABF, enhancing mass transport of NPs at the vessel-tissue interface (left), and swarms of MTB generating convective flow to improve mass transport (right). ECM, extracellular matrix. (**B**) Schematic of magnetofluidic platform for NP mass transport studies using magnetically induced convection. The microfluidic chip is placed between the objective lens of an inverted optical microscope and the electromagnets (left). A schematic depicts the chip, consisting of an upper channel filled with NPs (red) and a lower water channel (blue) that both border a collagen matrix (gray) along restricting trapezoidal posts made of PDMS. NPs can passively diffuse into the collagen matrix along their concentration gradient toward the water channel.

RESULTS

Wireless control of ABF induces convective flow

Like bacteria that use one or more rotating flagella for their locomotion, many synthetic, helical-shaped swimmers, including the ABF, have been designed to replicate this motion for efficient propulsion at the microscale, where viscous drag forces dominate (*23*, *24*). In this study, magnetic ABFs were fabricated by three-dimensional (3D) lithography and metal deposition, as previously reported (fig. S1) (*25*). Because the ABF is able to manipulate micro-objects in a noncontact, fluidic-driven fashion (*26*), we hypothesized that wireless control of an ABF could locally alter convection to enhance transport of surrounding NPs. We started by testing the influence of an ABF on surrounding NPs as it was navigated through open micropools. The motion of the ABF was controlled via uniform magnetic fields rotating in 3D using a setup consisting of eight electromagnets arrayed around a single hemisphere (Fig. 1B) (*22*) and mounted atop an inverted microscope to track and record the movements of the controlled microrobot. By applying such rotating magnetic fields (RMFs), a continuous magnetic torque powered the ABF, resulting in forward propulsion and convective flow in the surrounding fluid. When the ABF was immersed in a suspension of fluorescent polystyrene NPs, we observed controlled, spatiotemporally confined flow via the associated mass transport of the surrounding NPs (movie S1).

ABF locally perturbs fluid flow

We next quantified the extent to which the motion of a rotating ABF in a vessel is expected to perturb fluid flow. For this purpose, we developed a numerical two-fluid flow model incorporating a rotating ABF. This model consists of a 200-μm-wide channel stream with two inlets for separately incoming fluids at a flow velocity of 50 μm/s to mimic the blood flow rates found in capillaries (*27*). The bottom fluid (red) contains 200-nm NPs, while the top fluid (blue) bears pure aqueous suspension medium (Fig. 2A). Mass transport of NPs could then be modeled analogously to a molecular species with a concentration of 1 mol/m³ in the bottom fluid, 0 mol/m³ in the top fluid, and a diffusivity consistent with 200-nm particles. NPs with these dimensions are the largest likely to be encountered in clinical applications (*28*), allowing the results of this model to be interpreted as a lower bound for the transport enhancement expected for smaller particles. The ABF was placed in the center of the channel and assigned a rotational velocity consistent with a forward motion countering the velocity of the incoming stream, thereby maintaining its position against the flow. That is, the ABF's forward motion was directed upstream (to the right), while the input fluid flow (downstream, to the left) counteracted the ABF's motion, resulting in its steady position at the center of the channel (Fig. 2A). The expected disruption of fluid flow produced by the rotating ABF and its impact on transporting NPs to the upper
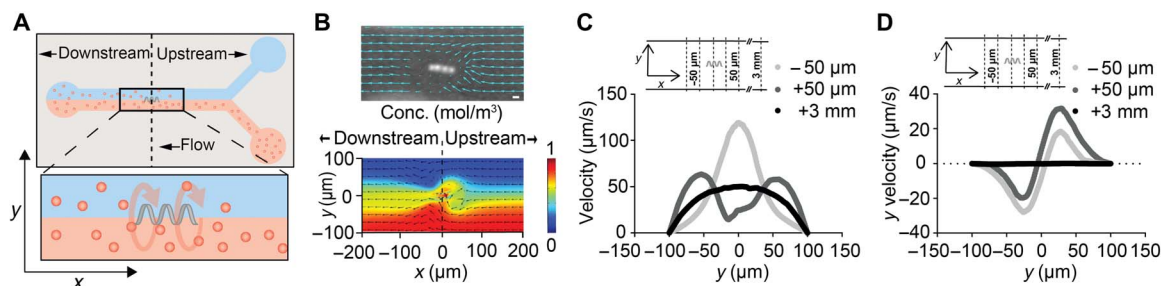
Fig. 2. ABF locally perturbs fluid flow. (A) Schematic of a 200-μm-wide microfluidic channel with suspended ABF (36 μm long, 10 μm in diameter) positioned at the channel center $(x,y,z) = (0,0,0)$. The upper channel contains water, whereas the lower channel contains 200-nm fluorescent NPs. **(B)** Snapshot of ABF in a 200-μm-wide channel perturbing the tracked paths of the 200-nm fluorescent NPs indicating fluid flow. Scale bar (top), 10 μm. A numerical simulation of two-fluid flow with an ABF at the interface, with color indicating concentration distribution (red, 1 mol/m³; blue, 0 mol/m³) of molecular species (bottom). **(C)** Velocity profile at positions upstream and downstream of the ABF. For the control, at $x = +3$ mm, an unperturbed laminar profile with peak velocity of 50 μm/s was simulated. At both $x = +50$ μm (upstream) and $x = −50$ μm (downstream), an increase in peak velocities is predicted, with the peak shifted closer toward the channel wall for the upstream case. **(D)** Simulation results for the y velocity component $\mathbf{u_y}$ (orthogonal to and out of the channel) at the same positions as (C). In the vicinity of the ABF, a push directed orthogonal to the flow direction toward the channel wall is predicted.

half of the channel was modeled (Fig. 2B). We observed a similar flow field experimentally in microfluidic devices (Fig. 2, A and B) that were modeled after those developed by Farahat and colleagues (29) and fabricated by means of polydimethylsiloxane (PDMS) soft lithography. As predicted, incoming fluids are mixed by the ABF, and NPs from the bottom stream are transported from the lower to the upper half of the channel, increasing the local concentration at the upper wall (fig. S2 and movies S2 and S3).

We next modeled and quantified the magnitude of the fluid velocity increase that the ABF introduces into this two-fluid flow model. Because the ABF must swim upstream, against the flow, to maintain its position at the center of the channel ($x = 0$), in the following discussion, positions in front of the ABF are referred to as "upstream" ($x > 0$), whereas positions further down the channel, behind the ABF, are noted as "downstream" ($x < 0$) (Fig. 2A). The incoming flow profile at the inlet was typical of undisturbed laminar fluid flow (measured 3 mm upstream of the ABF; Fig. 2C), but at distances ranging from 5 to 100 μm away from the ABF, the total fluid velocity increased and the laminar flow was disrupted both upstream and downstream of the ABF (Fig. 2C and fig. S3). For the former, a camel back–shaped flow profile with increased peak velocities toward the wall was predicted. Specifically, the y component $\mathbf{u_y}$, which is significant because it corresponds to the transport component orthogonal to the flow direction and toward the collagen tissue region, was drastically elevated in proximity to the ABF, both upstream and downstream (Fig. 2D and fig. S3). We quantified the fold change of $\mathbf{u_y}$ induced by the ABF over undisturbed flow, which is equivalent to the fold change of the y component of the local Péclet number P_y. The Péclet number, defined as $Pe = \frac{L \cdot u}{D}$, where L is the characteristic length, u is the flow velocity, and D is the diffusive constant, describes the ratio of the convective to the diffusive transport rate, allowing us to quantify the impact on local transport enhancement induced by the ABF. Velocity data for undisturbed laminar flow were extracted at a distance of 3 mm upstream of the ABF, far enough away from the disturbed flow regime to act as a control. The local Péclet number P_y was increased by up to 2000-fold at a distance of 50 μm upstream and downstream of the ABF (fig. S3). Our model shows that rotation of the ABF within a microfluidic channel disrupts laminar flow, producing convection that increases NP concentration at the channel wall.

Bacteria-inspired microrobot amplifies NP transport

After using the two-fluid flow model to elucidate the effect of ABF rotation on mixing and transport inside channels, we next sought to theoretically and empirically analyze ABF-driven NP transport into tissue using a one-fluid flow model in a channel with a scale and fluid flow rate comparable to a microvessel (Fig. 3A). The microfluidic model consisted of either a 50- or 200-μm microchannel running alongside a central compartment filled with concentrated collagen that mimicked the dense network of fibers normally present in the extracellular matrix of vessel-surrounding tissue. A series of 150-μm-wide trapezoidal posts along the border of the channel served to confine the collagen when it was injected into the device. The posts were spaced 100 μm apart, forming intermittent diffusive outlets between the posts (Fig. 3A). We simulated the expected concentration increase across the outlet areas over time in a 50-μm-wide channel and found that a rotating ABF should observably alter the expected NP concentration profile (Fig. 3B and Supplementary Text). Transport was modeled via both Eulerian and Lagrangian descriptions of the flow field. Whereas the first method revealed a symmetric extension of convective flow around the ABF into the tissue compartments that were modeled as highly viscous media, the second model indicated a larger effect behind the ABF, comparable to a wake effect pushing the NPs closer to the wall.

We then used our magnetofluidic control setup (Fig. 1B) to experimentally test whether magnetic manipulation of the ABF could enhance NP mass transport into an adjacent tissue-mimicking matrix, as predicted. A continuous laminar flow of fluorescently labeled polystyrene NPs was established in the top channel by controlling hydrostatic pressure gradients between the inlet pool, depicted on the right, and the outlet pool, depicted on the left. To produce a concentration gradient and to ensure that NPs were not driven into the matrix by hydrostatic pressure, water similarly flowed through a second channel on the opposite side of the collagen matrix. By applying an RMF, the ABF was steered upstream against the flow, and its position was maintained in the center of the upper channel, yielding a narrow position distribution of the microrobot at the center outlet (area 3; movie S4 and fig. S4).

To detect changes in NP transport brought about by the presence of the rotating ABF (Fig. 3C), we measured fluorescence intensity in the outlet areas of our microfluidic devices (Fig. 3D). Specifically,
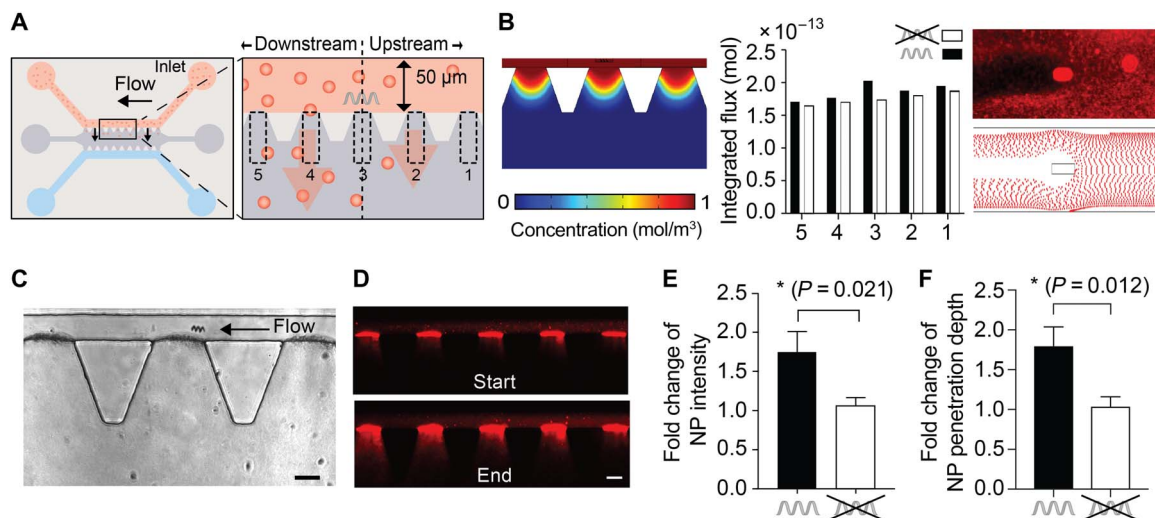
Fig. 3. ABF locally enhances NP transport. (**A**) Schematic of the microfluidic device (left) and conceptual sketch of experiment with numbered regions of interest, areas 1 to 5 (right). The ABF was controlled such that it maintained its position at the center of the channel (above area 3) by swimming upstream against the flow. (**B**) Simulated flux and simulated particle tracking in vicinity of the ABF. Left: Snapshot of the simulated concentration at three outlets upstream, downstream, and at the ABF. The bar graph in the middle quantifies the flux in the outlet areas for the five regions of interest in the vicinity of the ABF integrated over 1000 s (black) and for the same outlets in a control channel without ABF (white) based on Eulerian computational modeling. Right: A snapshot of an experiment showing the effect of the ABF on particle trajectories downstream (top) and a snapshot of such particle trajectories derived from Lagrangian computational modeling using the particle tracing interface in COMSOL Multiphysics. Although the effect of the ABF is captured as symmetric in fluid flow simulations based on Eulerian modeling, particle tracing simulation experiments indicate a slight asymmetry with stronger effects downstream of the ABF. (**C**) Bright-field image of an ABF in a microfluidic channel showing three outlets. (**D**) Fluorescence images at the beginning (top) and end (bottom) of an experiment, capturing the transport of 200-nm red fluorescent NPs into collagen. Scale bar, 50 μm. (**E**) Fold increase in fluorescence intensity of areas 2 to 5 compared to upstream control, area 1 ($n = 9$; *$P < 0.05$, Student's t test; ratio of mean intensity change over areas 2 to 5 to area 1). In the presence of a rotating ABF (black bar), a 1.75-fold increase in fluorescence intensity was measured. (**F**) Overall increase in penetration depth Δd was quantified by measuring the distance at which fluorescence intensity fell to $1/e$ of its maximum value at the channel wall at the start and end of the experiment. The mean penetration depth of areas 2, 3, 4, and 5 exhibited a 1.73-fold increase relative to area 1 ($n = 9$; *$P < 0.05$, Student's t test; ratio of mean penetration depth change over area 5 to 2 to area 1).

transport of NPs into collagen was recorded by time-lapse fluorescence imaging at two frames per second (fps), and the fluorescence intensity increase over time was quantified for each of five outlet regions in proximity to the ABF: two upstream (areas 1 and 2), two downstream (areas 4 and 5), and one at the position of the ABF (area 3; Fig. 3A). As suggested by our model, the outlet area furthest upstream of the ABF (area 1, equivalent to +500 μm) is expected to show the smallest increase of NP accumulation and was thus used as an internal baseline control. The areas directly upstream and downstream from the ABF experience increased flux due to convective flow induced by the ABF. In our experiments ($n = 9$), a mean increase in fluorescence intensity of 1.75 ± 0.26–fold (mean of areas 2 to 5) relative to the internal baseline (area 1) was observed, showing increased local NP accumulation (Fig. 3E and fig. S5). Control experiments ($n = 9$) were run without the ABF and showed no difference in NP distribution in these areas compared to the internal baseline (mean ratio = 1.06 ± 0.1), as expected for undisturbed, homogeneous diffusion.

Next, we analyzed whether not only total accumulation but also NP transport distance or penetration into the collagen matrix was influenced by the ABF. To do so, we measured the fluorescence signal as a function of the distance into the collagen matrix from the microchannel wall, the point of extravasation (fig. S6). Comparing the distance from the wall to the point at which measured fluorescence intensity dropped to $1/e$ of its maximum, we observed an increase in NP penetration depth of almost twofold in areas affected by the ABF relative to the unaffected area 1 (Fig. 3F).

We next considered whether the vessel diameter would have an effect on the magnitude of flow disruption induced by the ABF. Numerical simulations of channels with different sizes suggested that, in smaller vessels, greater increases in velocity in the y direction and toward the channel walls were achieved by the ABF (fig. S7). No significant change in NP concentration profiles was measured in experiments using larger channels of 200 μm (fig. S7). We hypothesized that this dependence on smaller channel sizes arises from the increased proximity of the rotating ABF surface to the low flow region in the vicinity of the vessel wall. By modeling the effect of ABFs of varying diameter in a vessel of constant size, we found that the effect of the ABF is most pronounced when it is closer to a wall (fig. S8). This observation limits the potential use of the ABF as a convective micropropeller to small vessels, although, in principle, one could scale the ABF according to the vessel size.

Controlled swarms of magnetically responsive bacteria enhance NP transport

Encouraged by clear evidence of enhanced transport observed in response to an individual ABF, which essentially functioned as a solitary intravascular propeller, we progressed to consider the effect of whole swarms of smaller microrobot propellers. This approach was motivated by the hypothesis that a distributed swarm could have an impact throughout the vasculature of a tissue, a strategy more far-reaching than an individual propeller and likely more suitable for application in larger vessels in vivo. However, difficulties in simultaneous control and the potential for agglomeration driven by magnetic interaction cast doubt on the feasibility of this approach.

Rather than deploying swarms of artificially synthesized miniature ABFs, we instead harnessed naturally occurring magnetic organisms, which act as magnetically manipulable structures. For this, we selected wild-type MTB, strain AMB-1 [*Magnetospirillum magneticum*, American Type Culture Collection (ATCC) 700264], which form magnetosomes (Fig. 4A), naturally produced chains of iron oxide particles contained in a lipid bilayer, that enable responsiveness of the bacteria to external magnetic fields (*30*). Several bacteria strains have already been proposed for use in cancer therapy, owing to their ability to home to tumors and colonize diseased tissue sites (*31*). Among these, MTB have previously been explored as potential cancer drug delivery vehicles, as they inherently disperse well in solutions without forming magnetic aggregates and their orientation can be controlled using external magnetic fields slightly higher than Earth's magnetic field (*21*). Instead of directing their natural swimming, we sought to coerce the collective movement of a swarm of MTB by applying RMFs that drive motion by imposing a magnetic torque.

AMB-1 is a bidirectional strain, meaning it has two flagella, one at each end of its elongated cell body. Upon exposure to an externally applied, directing magnetic field, these bacteria align with the field vector but may travel in either direction, hampering their efficient control with directing magnetic fields compared to unidirectional strains (movie S5). When subject to rotational magnetic fields, isolated bacteria of strain AMB-1 propel themselves along circular trajectories with radii corresponding to the frequency of the magnetic field rotation (Fig. 4B and fig. S9). As frequency is increased, the radii of their circular paths become progressively smaller until finally the bacteria are spun around their axes by the RMF, their own propulsion effectively overridden. While isolated bacteria spin in place under rotational fields, such motion in a dense swarm is capable of creating a translational flow due to hydrodynamic coupling, for which we saw a strong effect when RMFs were applied out of plane with respect to the surface boundary (Fig. 4C and movies S6 and S7). While rotating around their axes, MTB translated forward along the surface and on layers above, creating a volumetric net flow. A similar effect has been described for ferrofluids,

which are synthetic colloidal suspensions composed of small ferro- or ferrimagnetic NPs similar to the ones MTB synthesize naturally (*32, 33*). In such a fluid, viscous drag gives rise to a phase lag in the response of its magnetization such that a dipole torque is continuously exerted on each magnetic object under RMFs. At sufficient concentrations, these viscous forces ultimately yield a translational motion of the ferrofluid along solid interfaces guided by the direction of rotation of the magnetic field. The large magnetic moment of the chains of magnetic particles in the bacteria, as well as the hydrodynamic interaction that results from their nonmagnetic constituents, enables us to produce a torque-driven flow using only the RMF. Like "bacterial carpets" (*34*), this method makes use of bacteria to produce flow at an interface; however, here, the bacteria are not affixed, and the movement of the fluid is driven by externally applied magnetic forces rather than intrinsic flagellar motion.

We designed an experiment to test whether NP transport could be influenced by the convective flow associated with the coerced motion of MTB swarms exposed to external RMFs. We suspended MTB in a solution of fluorescent tracer NPs, allowing us to analyze fluid velocities and flow patterns under applied RMFs through particle velocimetry imaging. The applied RMF with frequency ω caused all bacteria to rotate synchronously about the y axis at the same rate ω (fig. S9). Under these conditions, bacteria were propelled out of their swimming plane, which, similar to effects observed for particle strings and clusters formed from colloidal suspensions (*35, 36*), resulted in forward motion along the surface. We observed an increase of translational velocity with increasing rotational frequency of the magnetic field up to a maximum value ω_{max}, at which the associated viscous torque is equal to the maximum available applied magnetic torque (Fig. 4D). Because the available magnetic torque is proportional to the applied field magnitude, ω_{max} shifts to larger values for higher RMF magnitudes. We also observed that the effect strengthens at higher swarm densities and weakens or vanishes as distances to nearest neighbors increase (fig. S10). At high concentrations of MTB, the average distance between bacteria is low, and neighbors can transmit
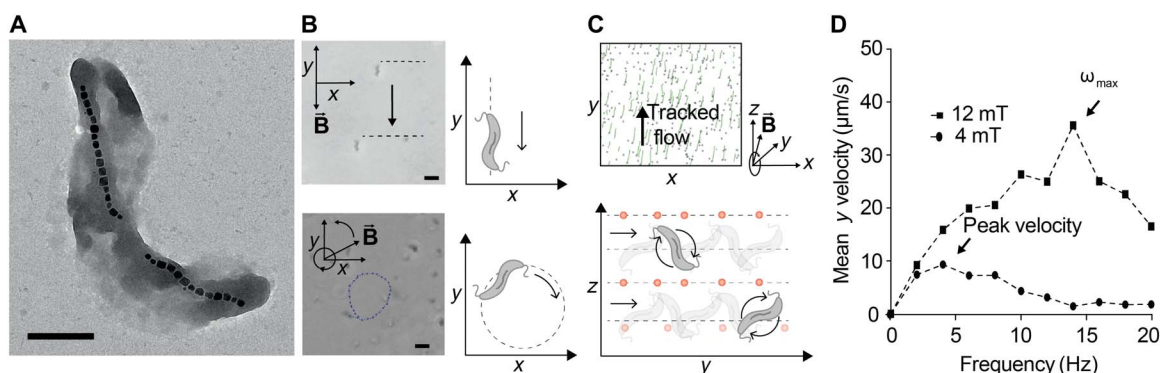

Fig. 4. Ferrohydrodynamic pumping with controlled swarms of MTB. (**A**) Transmission electron micrograph of *M. magneticum* strain AMB-1. Scale bar, 0.5 μm. The magnetosomes are clearly visible, here formed in two distinct strings of iron oxide crystals. (**B**) Control of AMB-1 under static magnetic fields (top) and magnetic fields rotating in-plane at 1 Hz. Scale bar (bottom), 5 μm. (**C**) Postprocessed images of tracked, cosuspended, nonmagnetic, fluorescent NPs used to observe flow fields generated by a swarm of MTB exposed to a 12-mT magnetic field rotating at 10 Hz in the *y-z* plane. Traces in green correspond to traveled trajectories over 12 frames (~1 s). Positions are computed using band-pass filter with 25-pixel diameter, followed by peak finding (top). Bacterial motion can be steered by changing the direction of the vector of the rotating magnetic field, because the MTB translate within the plane of rotation (bottom). For an RMF vector around the *x* axis, bacteria rotate along *y*, generating a flow that transports NPs along *y*. (**D**) Translational velocity is plotted versus applied rotational frequency at two different magnetic field strengths. Translational velocity increases with frequency initially, but at sufficiently high frequencies, it decreases because fluidic drag torque overcomes the magnetic torque to prevent them from keeping up with the rotation of the field. The maximum synchronized frequency, also corresponding to the maximum translational velocity, is referred to as the step-out frequency ω_{max}. When the magnetic field strength is increased, the step-out frequency increases, as observed.

forces to one another through boundary effects, thus yielding forward motion of swarms in 3D. In contrast to common synthetic colloidal magnetic suspensions, where magnetic particle-particle interactions dominate (36), this system is dominated by hydrodynamic forces. The magnetosomes are inherently well shielded from each other by the bacterial membrane (Fig. 4A), preventing interactions and clustering. This control scheme not only allows robust control of the translational motion of bidirectional swarms but also represents an attractive method to induce controlled fluid flow with MTB (movies S8 and S9).

On the basis of these findings, we proceeded to test whether magnetic actuation of MTB swarms could enhance NP transport into collagen in the same microfluidic devices used in our ABF experiments. To test this hypothesis, we flowed a mixture of MTB and fluorescent NPs through the microchannel, initiated an RMF to apply continuous magnetic torque, and quantified NP accumulation in five outlet areas (Fig. 5A). Because of the homogenous distribution of MTB along the channel, significant variation in accumulation between outlets was neither expected nor observed (fig. S11), in contrast to accumulation experiments with ABF performed in the same microfluidic devices (figs. S4 and S5). Experiments were run for 120 min under RMFs (+RMF; 5 mT and 6 Hz) and compared to control experiments without actuation (Fig. 5B). A low field magnitude of only 5 mT, paired

with a frequency of 6 Hz to reach peak velocities at the given field magnitude, was chosen to allow continuous operation of the coils without heating. A significant increase in overall NP accumulation was observed in experiments with magnetic field exposure (+RMF) versus those without (−RMF) (Fig. 5, B and C). The initial fluorescence intensity increase (normalized to start) per unit time over the first 10 min, corresponding to the flux rate of NPs into the collagen, increased by threefold for experiments with actuation (Fig. 5D). Moreover, the relative penetration depth was found to significantly increase as well (Fig. 5E).

Because active transport should lead to increased concentration relative to diffusive equilibrium, we also examined the influence of NP transport driven by the coerced motion of MTB swarms initiated after the onset of diffusive saturation. In these experiments, MTB and co-delivered NPs flowed through the channel for 60 min, followed by the application of RMFs for an additional 60 min. The fluorescence intensity in the collagen area below the channel began to plateau in the absence of actuation but increased immediately with the application of an RMF, exceeding diffusive equilibrium (Fig. 5F). We quantified this effect by calculating the rate of change of absolute fluorescence intensity, which is proportional to NP flux into the collagen, between the 10 min (20 frames) before and after actuation. This rate increased slightly, although not significantly, immediately after the rotating
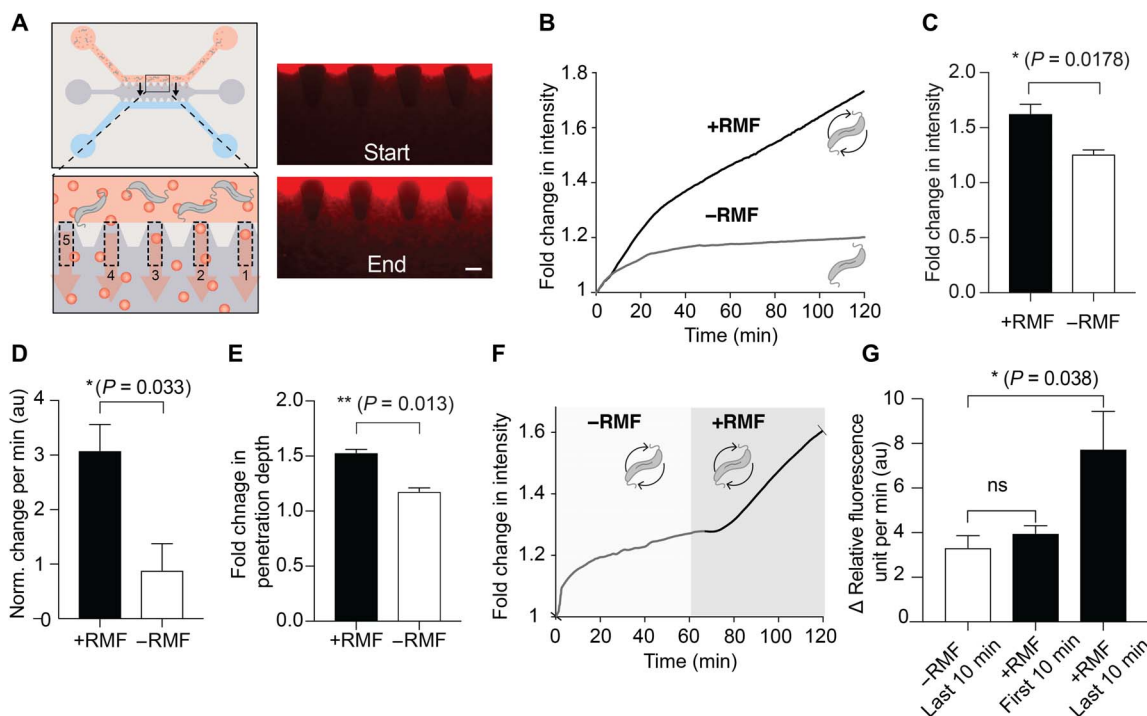

Fig. 5. Swarms of bacteria enhance NP transport. (**A**) Overview of NP transport experiment with MTB (top). Because MTB were spatially distributed across the channel, a homogenous increase across all five regions of interest was observed, as shown in the fluorescence images at the start and end of an experiment (t = 120 min). Scale bar, 100 μm. The intensity data were summed over all five outlets for analysis. (**B**) Sum of fluorescence intensity increase in all five outlets over time for MTB-NP transport without RMF (−RMF) and with RMF (+RMF; 5 mT and 6 Hz). (**C**) The normalized increase in fluorescence intensity over 120 min, relative to the initial intensity at t = 0, was measured to be a 1.63-fold increase for +RMF compared to a 1.26-fold increase for −RMF (n = 3; *P < 0.05, Student's t test). (**D**) The initial slope, in terms of fluorescence intensity increase per time (normalized to the start), was threefold higher for experiments without actuation (n = 3; *P < 0.05, Student's t test, over 20 frames). au, arbitrary units. (**E**) Relative penetration depth also increased in the presence of RMF actuation (n = 3; **P < 0.05, Student's t test). (**F**) Fluorescence intensity increase versus time for reinitiation of NP transport exceeding diffusive equilibrium. An RMF is applied after a delay of 60 min (shaded region). (**G**) The rate of change of fluorescence intensity increased slightly, although not significantly, within the first 10 min upon magnetic field initiation (n = 5; P > 0.05, Student's t test) but then rose 2.3-fold compared to the rate of change of fluorescence intensity in the last 10 min without bacterial actuation (n = 5; *P < 0.05, Student's t test). ns, not significant; RFU, relative fluorescence units.

field had been initiated but eventually rose to a level 2.3-fold higher in the segment of the last 10 min with actuation (+RMF), compared to the last 10 min without actuation (−RMF; Fig. 5G). While we were primarily focused on the transport of nonmagnetic companion NPs, we also observed MTB in the collagen area, suggesting that the applied magnetic torque may support their penetration into the matrix (movie S10). Another possible advantage of using MTB is that swarms can be controlled in an open loop fashion without the need for tracking. While hurdles remain to be overcome before practical application of the simultaneous imaging, actuation, and tracking of microrobots could be put in place, MTB such as those presented here could be injected into circulation, while RMFs are applied at the diseased site, and lead both bacteria and companion NPs to penetrate deeper into tissue, provided that sufficient concentrations of bacteria can be obtained.

DISCUSSION

This work explored two strategies to enhance mass transport of NPs using convective flow generated by magnetically controlled micropropellers. The first of these strategies used an ABF, a microfabricated magnetic structure mimicking a bacterial flagellum in its shape and function. Numerical modeling suggested that a single ABF rotating in intravascular-like flow introduces convection that transports companion NPs within the vessel, leading them to accumulate at the vessel wall and penetrate into adjacent tissue. Experiments using a microfluidic model of the vessel-tissue interface validated this prediction of enhanced transport and demonstrated that the ABF influenced the increase of NP accumulation and penetration into a dense collagen matrix. These results indicate that locally controlled convective flow can be generated by such magnetic micropropellers introduced into microfluidic devices when acted upon by RMFs. While several obstacles would still need to be overcome for practical implementation of imaging and control of such a microrobot in vivo, the convective effects of the ABF may prove useful in vascular implants with incorporated drug release. For example, stationary ABFs could potentially be integrated into stents to trigger drug release and enhance penetration counteracting inflammation on demand.

The second strategy focused on generating volumetric convective flow with the same magnetic stimulus, this time adopting bacteria themselves as magnetically manipulable objects. In contrast to simply directing the natural motion of MTB, RMFs were shown to override native locomotion and even generate translation in immotile MTB when present in sufficiently dense swarms. MTB swarms were found to create expansive convective flow fields that, when tested in the same microfluidic model as the ABF, increased NP accumulation, extended penetration depth, and caused NP transport to exceed the limits of diffusive saturation. Our observations of MTB penetrating the collagen matrices, as well as the tumor-homing properties of MTB, together suggest that magnetic control and enhanced NP transport within the tumor microenvironment may be feasible. The results of our microfluidic models further suggest that to promote enhanced NP transport in the tumor, a very high concentration of bacteria would be required, and these density levels may be difficult to achieve in vivo. However, this challenge may be surmountable, given the potential for bacterial proliferation in the tumor environment. Indications of penetration of bacteria into the collagen matrix support the idea that small compartments in the interstitial fluid space of a tumor microenvironment could be populated. We speculate that flow generated by even comparatively few bacteria in such spaces may be sufficient

to influence NP transport, as shown in transport experiments carried out in smaller compartments (fig. S10C). Furthermore, shear forces that are locally produced by rotating bacteria could promote cellular uptake of NPs (37). Another beneficial aspect of using such bacterial swarms in a clinical setting is that spatial tracking is not required. RMFs could be applied throughout the tumor tissue with random orientations for predetermined time intervals. Ultimately, coadministration of magnetically responsive MTB and drug-loaded NPs could provide an approach for improved drug delivery into diseased tissue sites.

Both rotating ABFs and controlled ferrohydrodynamic effects by swarms of MTB may also serve as attractive options to control local convective flow in laminar flow–determined microfluidics. Our integrated magnetic control and imaging platform was essential in the development and testing of our actuation strategies and could pave the way for further studies of micro- and nanomaterials for magnetically enhanced transport.

MATERIALS AND METHODS
Fabrication and actuation of ABF
The ABF was fabricated by two-photon photopolymerization using a 3D laser lithography system (Nanoscribe). On one 2-cm large circular glass wafer, an array of 8×6 clusters containing 8×20 structures of 36 μm in length and 10 μm in diameter were written into IP-L photoresist. A nickel-titanium bilayer was sputtered onto the structures to magnetize them before they were released from their substrate and suspended in water by ultrasonication in a water bath for 2 min. The complete release from the glass substrate was subsequently visually confirmed under the microscope. The ABF suspension was collected and concentrated to approximately two ABF per 1 μl. By applying a uniform RMF through our electromagnetic control setup, the ABF was then powered through the application of magnetic torque resulting from the misalignment of the external magnetic field vector **B** and the magnetic moment vector **M** of the ABF. Rotating the magnetic field vector **B** in a plane perpendicular to the helical axis thus controlled both the direction and speed of the ABF and resulting microflow. While the ABF is able to create microvortices regardless of swimming direction, it can only be kept stationary by being directed upstream and matching the flow rate.

Microfluidic device fabrication
The microfluidic devices consisted of a PDMS layer bonded to a glass slide. The PDMS layer was fabricated by soft lithography of a master created with 100-μm-thick negative photoresist (SU-8, MicroChem) patterned onto a silicon wafer by photolithography (Fig. 2). PDMS was prepared by mixing prepolymer base and cross-linker (SYLGARD 184 Silicone Elastomer Kit, Dow Corning) at a 10:1 ratio. Following vacuum degassing, the mixture was poured into the master and molded at 80°C for at least 2 hours. Pieces of the PDMS layer corresponding to individual devices were carefully cut out. Holes of different diameters (12 mm for the collagen gel channels and 8 mm for the fluidic channels; Fig. 1) were made by punching through the PDMS with Uni-Core biopsy punchers. After cleaning and oxygen plasma treatment, each PDMS piece was bonded to a glass slide (Thermo Scientific) and allowed to rest for at least 12 hours before use.

For NP transport studies, each microfluidic device consisted of three channels: one 1-mm-wide central region bordered by an array

of 150-μm-wide trapezoidal PDMS posts arranged in 100-μm intervals, into which a collagen gel solution was loaded, and two 50- or 200-μm-wide side channels, one of which was filled with NP-ABF or NP-MTB suspension and the second of which was filled with water (Fig. 1). A collagen type I solution (3 mg/ml) was prepared as described previously (38, 39) and loaded into the central region. Filled devices were incubated at 37°C and 5% CO_2 overnight to allow the collagen to gel.

For MTB transport studies, each microfluidic device consisted of a 20-μm-deep pool or channel, into which two holes of 10 mm diameter were cut and a dense MTB suspension [optical density (OD) ~ 1] in phosphate-buffered saline was loaded.

Wireless magnetic control setup

We used a small-scale electromagnetic manipulation system consisting of eight electromagnets arranged in a single hemisphere (22). The system was integrated with an inverted microscope (Nikon Ti Eclipse), as well as a multiphoton microscope (Olympus FV1000 multiphoton laser scanning confocal microscope). The configuration provides a 2-cm working distance, making it compatible with microfluidic devices, cell and tissue samples, as well as animal in vivo studies. The sample is located between the lens and the eight electromagnets (Fig. 1). The system can generate arbitrary 3D magnetic fields up to 50 mT in magnitude and gradients up to 5 T/m and can operate at a maximum frequency of 2 kHz.

In silico studies using COMSOL Multiphysics

A mathematical model was created to study the induced local convection of a single rotating microstructure and its effect on concentration distribution of a molecular component by using the Fluid Flow and Transport of Diluted Species modules in COMSOL. The geometric setting of the simulation entails a flow channel with two inflow conditions and one outflow condition. The inflow condition is set to a laminar inflow, and the fluid is assumed to be incompressible with a constant viscosity and density ($\eta = 8.9 \times 10^{-4}$ Pa s, $\rho = 1$ g/cm^3). Channel walls were described with a zero-velocity fluid, i.e., no slip, condition. The interior wall condition ensured a smooth transition between two domains by assigning the same velocity at contact. The inflow and outflow conditions were set to yield the fluid velocities and the pressure at the respective boundaries to create the flow inside the model. A moving wall boundary condition described the interior wall in motion. Therefore, the no slip wall condition was adapted to the velocity of the wall. Further details on modeling of the NP transport into collagen can be found in Supplementary Text.

ABF-NP magnetofluidic transport experiments

An aqueous solution of NPs (red fluorescent FluoSpheres carboxylate-modified microspheres, 0.2 μm; excitation/emission, 580/605 nm) was prepared at a 50:1 ratio. Collagen-loaded microfluidic devices with a channel width of 200 μm (for both one-phase and two-fluid flow) or 50 μm (for one-phase flow) were used in these studies. Before loading, devices were equilibrated by loading the wells for each of the flanking channels with water, applying negative pressure to fill the channel, and allowing them to rest for 5 min. Water was then aspirated from the flanking channels. NP suspension (80 μl) was loaded into one well, and 10 μl of ABF suspension and 40 μl of deionized water were loaded into the second well. The loaded device was then positioned in the imaging stage under the wireless magnetic control setup described above. We observed a flow of approximately 15 to 50 μm/s under

the microscope and applied alternating magnetic fields to detect an ABF in the inlet pool area. Once identified, the spinning vector was aligned with the axis of the ABF, the frequency was adjusted to transition from tumbling (low frequency) to swimming motion, and the ABF was steered into the microchannel (movie S4). A section of five PDMS posts and outlets on the device that were similar in collagen integrity and NP diffusion pattern was imaged at ×10 magnification at two frames per minute, where the ABF was actuated at 5 to 10 mT and the appropriate frequency so that its position was maintained above the central PDMS post. The ABF was imaged under magnetic actuation for up to 20 min, and results were normalized by time. Control studies were conducted by loading the collagen devices as described above with 50 μl of deionized water in replacement of the ABF suspension and then by imaging a section of five PDMS posts for up to 20 min.

MTB culture conditions

Cultures of M. magneticum sp. AMB-1 were grown in magnetic spirillum growth medium (ATCC® Medium 1653) containing the following per liter: 5.0 ml of Wolfe's Mineral Solution (ATCC), 0.68 g of potassium phosphate, 0.12 g of sodium nitrate, 0.035 g of ascorbic acid, 0.37 g of tartaric acid, 0.37 g of succinic acid, and 0.05 g of sodium acetate. The final pH was adjusted to 6.75 with NaOH before autoclaving. Wolfe's Vitamin Solution (100×) (ATCC) and 10 mM ferric quinate (200×) were added to the culture media before use. Cultures were grown anaerobically at 30°C and passaged every 3 to 5 days.

MTB-NP magnetofluidic transport experiments

Bacteria were cultured until a large, dark pellet formed at the base of the culture tube. The magnetic responsiveness of the bacteria was assessed with a permanent magnet and with measurements of the magnetic dependence of the optical density (40). Bacteria were resuspended in culture media and centrifuged at 8000 rpm for 5 min. Media were aspirated, and bacteria were resuspended in phosphate-buffered saline to an OD_{550} of approximately 1. A solution of NPs and MTB was prepared at a dilution of 1:50. A collagen-loaded microfluidic device with a channel width of 50 or 200 μm was used in these studies. Before loading, devices were equilibrated by loading the wells for each of the flanking channels with water, applying negative pressure to fill the channel, and allowing them to rest for 5 min. Water was then aspirated from one of the two flanking channels. MTB-NP suspension (80 μl) was loaded into one well, and 20 μl of MTB-NP suspension was loaded into the second well. The loaded device was then positioned in the imaging stage under the wireless magnetic control setup described above (Fig. 1). The area over five PDMS posts and outlets on the device was imaged at ×10 magnification at two frames per minute. For amplification experiments, a loaded device was imaged for 120 min without magnetic actuation, and a second device, loaded with the same batch of MTB-NP suspension, was subsequently imaged for 120 min under magnetic actuation at 5 mT and 6 Hz. For saturation recovery experiments, the loaded device was imaged for 60 min without magnetic actuation, after which magnetic actuation was initiated and the same device was imaged for an additional 60 min.

Postprocessing of NP transport recordings

All image and video postprocessing was performed in MATLAB. For the ABF-NP transport studies, five regions of interest were defined within each frame for evaluation of fluorescence intensity in the collagen matrix. Each region had a width of 170 pixels and a height of

400 pixels, with a pixel size of 0.65 μm. The upper bound in the y direction of all regions of interest was the same and was set immediately below the interface of the ABF-containing channel and collagen posts. The left and right bounds of the regions were defined so that each region captured the area of collagen between two given posts. A summation of fluorescence intensity within the regions of interest was performed for each frame. To calculate the penetration depth of NPs into the collagen matrix, the first element with fluorescence intensity smaller than $1/e$ of the fluorescence intensity at the collagen post in the first and last frames of the experiment was identified. Penetration depth was defined as the difference between the $1/e$ cutoff distance at the end of the experiment and that of the start. On the basis of our simulations, outlet areas 2 to 5 were considered to be affected by ABF actuation, and the mean of the overall fluorescence increase of these four areas was calculated and compared to the increase in area 1, the area farthest upstream of the ABF, which was considered to be unaffected by ABF actuation.

For the MTB-NP transport studies, a single region of interest that captured the collagen matrix was defined. The upper bound was set at the interface between the MTB-NP channel and the collagen posts, with a region width of 2400 pixels and length of 800 pixels. The penetration depth of NPs into the collagen matrix was calculated, as described before for the ABFs with a $1/e$ fluorescence intensity cutoff. For amplification experiments, the slope across the first 20 frames and last 20 frames of each experiment (with or without magnetic actuation) was determined. For saturation recovery experiments, slope changes in intensity over time curves were determined by taking the mean of intensity change between consecutive frames across the last 20 frames immediately before magnetic actuation was initiated, as well as across 20 frames immediately after magnetic actuation of MTB was initiated.

Characterization of bacterial ferrohydrodynamics

To quantify the velocity fields derived during bacterial ferrohydrodynamic transport experiments, we tracked MTB by particle tracking velocimetry using an IDL particle tracking algorithm translated into MATLAB, while tracking of NPs was performed using particle image velocimetry (PIV) with the MATLAB PIVlab toolkit. MTB velocities were manipulated by altering the magnetic field strength in increments of 4 mT, the magnetic field frequency in increments of 10 Hz, and the direction of the spinning vector of the RMF. Trajectories were recorded at 12 fps under a Nikon Ti Eclipse 20× objective. For MTB tracking, positions at each frame were computed using a band-pass filter with 25-pixel diameter, followed by peak finding. Trajectories were then computed using a particle tracking algorithm developed originally in IDL (41) and translated into MATLAB by D. Blair and E. Dufresne. For NP tracking, frame pairs were imported into PIVlab and 19 velocity vectors were computed along each axis for each frame pair. The PIV settings used were a first-pass interrogation area of 256 pixels by 256 pixels with a step size of 128 pixels and a second pass interrogation area of 192 pixels by 192 pixels with a step size of 64 pixels. Manual vector validation was performed following the calculation of velocity fields for all of the frames to remove outliers before computing mean x and y velocities for each frame. A total of 50 frames of video were used to compute the mean x and y velocity for each set of magnetic field parameters used.

Statistics and data analysis

All statistical analyses were performed in GraphPad (Prism 5.0). Statistical significance and individual tests are described in figure legends.

SUPPLEMENTARY MATERIALS

REFERENCES AND NOTES

1. J. Shi, P. W. Kantoff, R. Wooster, O. C. Farokhzad, Cancer nanomedicine: Progress, challenges and opportunities. Nat. Rev. Cancer 17, 20–37 (2017).
2. R. Tong, R. Langer, Nanomedicines targeting the tumor microenvironment. Cancer J. 21, 314–321 (2015).
3. E. Blanco, H. Shen, M. Ferrari, Principles of nanoparticle design for overcoming biological barriers to drug delivery. Nat. Biotechnol. 33, 941–951 (2015).
4. S. Wilhelm, A. J. Tavares, Q. Dai, S. Ohta, J. Audet, H. F. Dvorak, W. C. W. Chan, Analysis of nanoparticle delivery to tumours. Nat. Rev. Mater. 1, 16014 (2016).
5. P. Koumoutsakos, I. Pivkin, F. Milde, The fluid mechanics of cancer and its therapy. Annu. Rev. Fluid Mech. 45, 325–355 (2013).
6. R. Toy, P. M. Peiris, K. B. Ghaghada, E. Karathanasis, Shaping cancer nanomedicine: The effect of particle shape on the in vivo journey of nanoparticles. Nanomedicine 9, 121–134 (2014).
7. B. R. Smith, P. Kempen, D. Bouley, A. Xu, Z. Liu, N. Melosh, H. Dai, R. Sinclair, S. S. Gambhir, Shape matters: Intravital microscopy reveals surprising geometrical dependence for nanoparticles in tumor models of extravasation. Nano Lett. 12, 3369–3377 (2012).
8. C. Wong, T. Stylianopoulos, J. Cui, J. Martin, V. P. Chauhan, W. Jiang, Z. Popović, R. K. Jain, M. G. Bawendi, D. Fukumura, Multistage nanoparticle delivery system for deep penetration into tumor tissue. Proc. Natl. Acad. Sci. U.S.A. 108, 2426–2431 (2011).
9. S. Hauert, S. Berman, R. Nagpal, S. N. Bhatia, A computational framework for identifying design guidelines to increase the penetration of targeted nanoparticles into tumors. Nano Today 8, 566–576 (2013).
10. J. M. Morachis, E. A. Mahmoud, A. Almutairi, Physical and chemical strategies for therapeutic delivery by using polymeric nanoparticles. Pharmacol. Rev. 64, 505–519 (2012).
11. J. Owen, Q. Pankhurst, E. Stride, Magnetic targeting and ultrasound mediated drug delivery: Benefits, limitations and combination. Int. J. Hyperthermia 28, 362–373 (2012).
12. W. Tzu-Yin, K. E. Wilson, S. Machtaler, J. K. Willmann, Ultrasound and microbubble guided drug delivery: Mechanistic understanding and clinical implications. Curr. Pharm. Biotechnol. 14, 743–752 (2013).
13. S. Barua, S. Mitragotri, Challenges associated with penetration of nanoparticles across cell and tissue barriers: A review of current status and future prospects. Nano Today 9, 223–243 (2014).
14. S. Erni, S. Schuerle, A. Fakhraee, B. E. Kratochvil, B. J. Nelson, Comparison, optimization, and limitations of magnetic manipulation systems. J. Microbio Robot. 8, 107–120 (2013).
15. B. J. Nelson, I. K. Kaliakatsos, J. J. Abbott, Microrobots for minimally invasive medicine. Annu. Rev. Biomed. Eng. 12, 55–85 (2010).
16. J.-W. Yoo, D. J. Irvine, D. E. Discher, S. Mitragotri, Bio-inspired, bioengineered and biomimetic drug delivery carriers. Nat. Rev. Drug Discov. 10, 521–535 (2011).
17. H. Ceylan, J. Giltinan, K. Kozielski, M. Sitti, Mobile microrobots for bioengineering applications. Lab Chip 17, 1705–1724 (2017).

18. Y. Mardor, O. Rahav, Y. Zauberman, Z. Lidar, A. Ocherashvili, D. Daniels, Y. Roth, S. E. Maier, A. Orenstein, Z. Ram, Convection-enhanced drug delivery: Increased efficacy and magnetic resonance image monitoring. *Cancer Res.* **65**, 6858–6863 (2005).

19. A. Jahangiri, A. T. Chin, P. M. Flanigan, R. Chen, K. Bankiewicz, M. K. Aghi, Convection-enhanced delivery in glioblastoma: A review of preclinical and clinical studies. *J. Neurosurg.* **126**, 191–200 (2017).

20. L. Zhang, J. J. Abbott, L. Dong, B. E. Kratochvil, D. Bell, B. J. Nelson, Artificial bacterial flagella: Fabrication and magnetic control. *Appl. Phys. Lett.* **94**, 064107 (2009).

21. O. Felfoul, M. Mohammadi, S. Taherkhani, D. de Lanauze, Y. Z. Xu, D. Loghin, S. Essa, S. Jancik, D. Houle, M. Lafleur, L. Gaboury, M. Tabrizian, N. Kaou, M. Atkin, T. Vuong, G. Batist, N. Beauchemin, D. Radzioch, S. Martel, Magneto-aerotactic bacteria deliver drug-containing nanoliposomes to tumour hypoxic regions. *Nat. Nanotechnol.* **11**, 941–947 (2016).

22. S. Schuerle, S. Erni, M. Flink, B. E. Kratochvil, B. J. Nelson, Three-dimensional magnetic manipulation of micro-and nanostructures for applications in life sciences. *IEEE Trans. Magn.* **49**, 321–330 (2013).

23. K. E. Peyer, S. Tottori, F. Qiu, L. Zhang, B. J. Nelson, Magnetic helical micromachines. *Chemistry* **19**, 28–38 (2013).

24. S. Schuerle, S. Pané, E. Pellicer, J. Sort, M. D. Baró, B. J. Nelson, Helical and tubular lipid microstructures that are electroless-coated with CoNiReP for wireless magnetic manipulation. *Small* **8**, 1498–1502 (2012).

25. S. Tottori, L. Zhang, F. Qiu, K. K. Krawczyk, A. Franco-Obregón, B. J. Nelson, Magnetic helical micromachines: Fabrication, controlled swimming, and cargo transport. *Adv. Mater.* **24**, 811–816 (2012).

26. K. E. Peyer, L. Zhang, B. J. Nelson, Localized non-contact manipulation using artificial bacterial flagella. *Appl. Phys. Lett.* **99**, 174101 (2011).

27. G. Zhang, *Computational Bioengineering* (CRC Press, 2015).

28. C. Dhand, M. P. Prabhakaran, R. W. Beuerman, R. Lakshminarayanan, N. Dwivedi, S. Ramakrishna, Role of size of drug delivery carriers for pulmonary and intravenous administration with emphasis on cancer therapeutics and lung-targeted drug delivery. *RSC Adv.* **4**, 32673–32689 (2014).

29. W. A. Farahat, L. B. Wood, I. K. Zervantonakis, A. Schor, S. Ong, D. Neal, R. D. Kamm, H. H. Asada, Ensemble analysis of angiogenic growth in three-dimensional microfluidic cell cultures. *PLOS ONE* **7**, e37333 (2012).

30. M. Büttner, P. Weber, C. Lang, M. Röder, D. Schüler, P. Görnert, P. Seidel, Examination of magnetite nanoparticles utilising the temperature dependent magnetorelaxometry. *J. Magn. Magn. Mater.* **323**, 1179–1184 (2011).

31. N. S. Forbes, Engineering the perfect (bacterial) cancer therapy. *Nat. Rev. Cancer* **10**, 785–794 (2010).

32. M. N. Zahn, P. Wainman, Effects of fluid convection and particle spin on ferrohydrodynamic pumping in traveling wave magnetic fields. *J. Magn. Magn. Mater.* **122**, 323–328 (1993).

33. L. Mao, S. Elborai, X. He, M. Zahn, H. Koser, Direct observation of closed-loop ferrohydrodynamic pumping under traveling magnetic fields. *Phys. Rev. B Condens. Matter* **84**, 104431 (2011).

34. N. Darnton, L. Turner, K. Breuer, H. C. Berg, Moving fluid with bacterial carpets. *Biophys. J.* **86**, 1863–1870 (2004).

35. A. van Reenen, A. M. de Jong, M. W. J. Prins, Transportation, dispersion and ordering of dense colloidal assemblies by magnetic interfacial rotaphoresis. *Lab Chip* **15**, 2864–2871 (2015).

36. M. Driscoll, B. Delmotte, M. Youssef, S. Sacanna, A. Doniv, P. Chaikin, Unstable fronts and motile structures formed by microrollers. *Nat. Phys.* **13**, 375–379 (2017).

37. Y. Zhang, J. Yu, H. N. Bomba, Y. Zhu, Z. Gu, Mechanical force-triggered drug delivery. *Chem. Rev.* **116**, 12536–12563 (2016).

38. B. M. Baker, B. Trappmann, S. C. Stapleton, E. Toro, C. S. Chen, Microfluidics embedded within extracellular matrix to define vascular architectures and pattern diffusive gradients. *Lab Chip* **13**, 3246–3252 (2013).

39. Y. Shin, S. Han, J. S. Jeon, K. Yamamoto, I. K. Zervantonakis, R. Sudo, R. D. Kamm, S. Chung, Microfluidic assay for simultaneous culture of multiple cell types on surfaces or within hydrogels. *Nat. Protoc.* **7**, 1247–1259 (2012).

40. L. Zhao, D. Wu, L.-F. Wu, T. Song, A simple and accurate method for quantification of magnetosomes in magnetotactic bacteria by common spectrophotometer. *J. Biochem. Biophys. Methods* **70**, 377–383 (2007).

41. J. C. Crocker, D. G. Grier, Methods of digital video microscopy for colloidal studies. *J. Colloid Interface Sci.* **179**, 298–310 (1996).

42. S. Ramanujan, A. Pluen, T. D. McKee, E. B. Brown, Y. Boucher, R. K. Jain, Diffusion and convection in collagen gels: Implications for transport in the tumor interstitium. *Biophys. J.* **83**, 1650–1660 (2002).